Effects of Three-Dimensional Photon Transport on the Radiative Forcing of Realistic Contrails

LINDA FORSTER, CLAUDIA EMDE, AND BERNHARD MAYER

Meteorologisches Institut, Ludwig-Maximilians-Universität, München, Germany

SIMON UNTERSTRASSER

Institut für Physik der Atmosphäre, Deutsches Zentrum für Luft- und Raumfahrt (DLR), Oberpfaffenhofen, Wessling, Germany

(Manuscript received 29 July 2011, in final form 30 December 2011)

ABSTRACT

Estimates of the global radiative forcing (RF) of line-shaped contrails and contrail cirrus exhibit a high level of uncertainty. In most cases, 1D radiative models have been used to determine the RF on a global scale. In this paper the effect of neglecting the 3D radiative effects of realistic contrails is quantified. Calculating the 3D effects of an idealized elliptical contrail as in the work of Gounou and Hogan with the 3D radiative transfer model MYSTIC (for ''Monte Carlo code for the physically correct tracing of photons in cloudy atmospheres'') produced comparable results: as in Gounou and Hogan's work the 3D effect (i.e., the difference in RF between a 3D calculation and a 1D approximation) on contrail RF was on the order of 10% in the longwave and shortwave. The net 3D effect, however, can be much larger, since the shortwave and longwave RF largely cancel during the day. For the investigation of the 3D effects of more realistic contrails, the microphysical input was provided by simulations of a 2D contrail-to-cirrus large-eddy simulation (LES) model. To capture some of the real variability in contrail properties, this paper examines two contrail evolutions from 20 min up to 6 h in an environment with either high or no vertical wind shear. This study reveals that the 3D effects show a high variability under realistic conditions since they depend strongly on the optical properties and the evolutionary state of the contrails. The differences are especially large for low elevations of the sun and contrails spreading in a sheared environment. Thus, a parameterization of the 3D effects in climate models would need to consider both geometry and microphysics of the contrail.

1. Introduction

The global radiative forcing (RF) of line-shaped contrails and contrail cirrus calculated by general circulation models (GCMs) exhibits a high level of uncertainty. These uncertainties arise mainly from the radiative transfer models used to calculate the contrail RF as well as from the contrail parameterization and its inherent assumptions employed to represent contrail properties for large grid boxes rather than for individual contrails.

A recent study by Frömming et al. (2011) quantified the uncertainties in estimating the contrail cover and RF of line-shaped contrails from the GCM-based approach of Ponater et al. (2002). They found that the contrail RF depends most sensitively on the mean optical depth resulting on the global scale, a simulated quantity that is difficult to be constrained from observations (Kärcher et al. 2009). The other key parameter, contrail coverage, is strongly dependent on crucial assumptions about the detection efficiency of observations used to calibrate regional coverage in the GCM. Depending on the assumptions on each parameter, the RF may vary by a factor of 2.5.

New contrail parameterizations (Burkhardt and Kärcher 2009) on the global scale account also for contrail cirrus (aged contrails that have lost their linear shape) and use prognostic equations to estimate the contrail spreading. By introducing this second type of contrail class on a global scale, the global contrail (including contrail cirrus) coverage and forcing is about one order of magnitude larger than that exerted solely by line-shaped contrails (Burkhardt and Kärcher 2011).

Corresponding author address: Linda Forster, Meteorologisches Institut, Ludwig-Maximilians-Universität, München, Germany.
E-mail: linda.forster@physik.uni-muenchen.de

DOI: 10.1175/JAS-D-11-0206.1

Moreover, the assumed crystal shape and assumptions about the overlap with natural water and ice clouds are important.

Further uncertainties in estimating the global contrail RF arise from the radiative transfer models used in GCMs. Clearly, all GCMs equipped with contrail parameterizations [ECHAM for Ponater et al. (2002) and Burkhardt and Kärcher (2009) and Hadley Centre Global Environmental Model version 2 (HadGEM2) for Rap et al. (2010)] use 1D approximations. In a recent intercomparison (Myhre et al. 2009) of various radiation models (from detailed line-by-line models to fast approaches with a few bands as usually employed in GCMs), differences in contrail RF of a factor of 2 between the individual radiation models have been found for the same specified contrail scene.

Although contrails have a different three-dimensional shape, they are generally treated in 1D approximations. Because of computational limitations it is not feasible to use 3D radiative transfer models online in global climate models or to evaluate the GCM output offline with them. The effects of 3D radiative transfer on the RF of line-shaped contrails can be assessed so far only in offline studies with a small number of contrail setups. Gounou and Hogan (2007, hereafter GH) published the first comprehensive study of the effect of horizontal photon transport in idealized contrails in the shortwave as well as in the longwave. Prior to that, only Schulz (1998) had investigated the effect of horizontal photon transport in the shortwave region on the albedo of a rather young (up to 30 min old) contrail without wind shear, simulated by a large-eddy simulation (LES) model. These simulations were initialized with a 15-min-old contrail resembling the geometry of the idealized contrail of GH. Since the model output after 4, 14, and 30 min was used, the contrails were still close to the idealized initialization.

In this study the effects of three-dimensional photon transport on the RF of line-shaped, more realistic contrails were examined in order to assess the uncertainty in the RF calculations made by applying 1D approximations in GCMs. An accurate calculation of the radiative forcing of contrails is a challenging task, since the upwelling solar and thermal irradiances have to be computed very accurately. The net RF of contrails is relatively small and is calculated by taking the difference between the upwelling radiation for a clear-sky atmosphere and for an atmosphere including a contrail. The calculation of the 3D effects on the RF is even more intricate, since the difference between a 1D independent column approximation (ICA) and a 3D calculation is even smaller. Small errors in the radiative transfer models could produce artifacts that might be misinterpreted as 3D effects.

GH used the SHDOM model (Evans 1998) for a respective study. SHDOM is based on a spherical harmonics discrete ordinate method that is quite sensitive to the choice of various numerical grids. GH's estimate of the 3D effect on contrail RF is on the order of 10% in each the longwave and shortwave spectrum. A recalculation of the experiments with a setup as close as possible to the setup in GH was done using the Monte Carlo code for the physically correct tracing of photons in cloudy atmospheres (MYSTIC; Mayer 2009). The results of this completely different approach to solve the radiative transfer were comparable to GH's findings.

GH suggested that the 3D effects on contrail RF could be parameterized. Such a parameterization should consider both geometry and microphysics of the contrail since they influence each other and determine the radiative 3D effects of the contrail. To create a firm basis for a parameterization, however, more realistic contrails need to be studied. Therefore we investigated the 3D effects on the RF of realistic contrails with and without wind shear to gain more general results. For this we used the meteorological and microphysical output data of a numerical contrail-to-cirrus (LES) model (Unterstrasser and Gierens 2010a).

2. Methods

a. Radiative transfer model

The radiative transfer was calculated using the libRadtran software package (Mayer and Kylling 2005). The libRadtran package provides different possibilities for an accurate treatment of Rayleigh scattering, molecular absorption, aerosols, and water and ice clouds, as well as surface albedo. Furthermore, libRadtran provides several solvers for the radiative transfer equation. For the simulations DISORT (for ''discrete ordinate technique'') (Thomas and Stamnes 1999) and the 3D MYSTIC (Mayer 2009; Emde and Mayer 2007) were applied. MYSTIC was used for the 3D calculations of radiative transfer both in the shortwave and in the longwave spectral region. For the sensitivity studies with the idealized contrail, as defined by GH, the independent column approximation (ICA) and the clear-sky calculations in the shortwave spectrum were done using the DISORT solver to save computational time and gain noiseless results. All other calculations were performed with MYSTIC. For the experiments with the realistic contrails all calculations were done with the MYSTIC model. Since MYSTIC creates all photon paths with a random number generator and because scattering and absorption are treated statistically as well, all values calculated with MYSTIC are denoted with a statistical

error of 2σ, where σ represents the standard deviation. This guarantees with a probability of 95.5% that the solution lies within the margin of uncertainty.

b. Optical properties

For the spectral integration a correlated-k absorption band model was applied. In the shortwave the parameterization by Kato et al. (1999) was chosen with 32 bands from 240 to 4600 nm, and in the longwave the parameterization by Fu and Liou (1993) with 12 bands from 4545 nm to 10 000 μm was used. The contrail optical properties were parameterized following Key et al. (2002) for wavelengths smaller than 3.4 μm. From 3.4 to 100 μm the parameterization by Yang et al. (2000, 2005) was chosen. The parameterizations are consistent between 0.2 and 100 μm and accurate for the calculation of spectral irradiances. For the simulations solid columns were assumed, whose effective radii may range between about 6 and 84 μm for this parameterization. For this reason, effective radii exceeding the lower or upper limit of this interval were set to the respective boundary values (this was applied only in the case of the realistic contrail; see section 2d). GH parameterized the ice particles' optical properties according to Yang et al. (2000) as solid columns in the shortwave. In the longwave, however, they used spherical ice crystals following Mie theory. For the simulations performed, a shortwave surface albedo of 0.15 and a longwave surface emissivity of 0.98 were assumed, according to the setting of GH.

c. Idealized contrail

For the comparative sensitivity study an idealized linear contrail was set up as close as possible to GH in order to examine whether the results can be reproduced with the MYSTIC radiative transfer model. The calculations with the idealized contrail were done using the atmospheric trace gas background concentrations of the U.S. Standard Atmosphere (Anderson et al. 1986). GH used the U.S. Standard Atmosphere of McClatchey et al. (1972). The additional assumptions for the mixing ratios of CO_2, CH_4, and N_2O from GH could not be adopted for the following simulations, as quantitative statements are missing in their publication.

The idealized contrail was set up in a 15-km-wide and 50-km-high 2D domain with a spatial resolution of 100 m in the vertical as well as in the horizontal direction and periodic boundary conditions. In the direct vicinity of the contrail a finer vertical resolution of 50 m was chosen. The idealized contrail was defined, identically to the parameterization of GH, as a cylinder with elliptical base, which is infinitely extended along the y axis as shown in Fig. 1. The contrail is defined by the following IWC distribution:

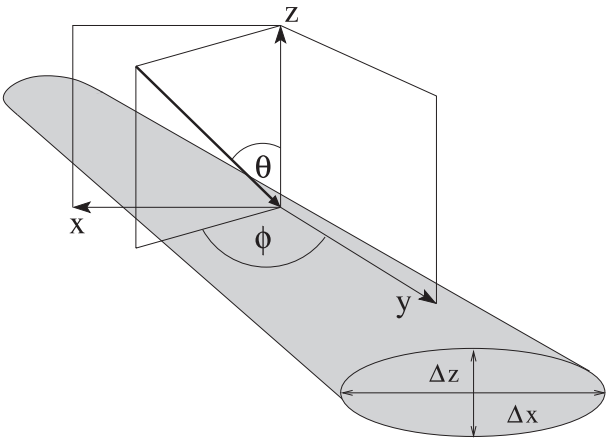

FIG. 1. Schematic sketch of the idealized contrail's position in the orthogonal coordinate system along the y axis. The orientation of the sun (thick arrow) with respect to the contrail is also illustrated. The position of the sun is determined by the solar zenith angle θ and the solar azimuth angle ϕ. The diameter of the contrail in the x and z directions are labeled with Δx and Δz, respectively.

$$\mathrm{IWC} = \begin{cases} \mathrm{IWC}_p \cos\left(\dfrac{\pi}{2} r\right) & \text{for} \quad r < 1, \\ 0 & \text{for} \quad r \geq 1, \end{cases} \tag{1}$$

where

$$r = \left[\left(\frac{x - x_0}{\Delta x/2} \right)^2 + \left(\frac{z - z_0}{\Delta z/2} \right)^2 \right]^{1/2}. \tag{2}$$

Here, Δx denotes the contrail's geometric width and Δz its geometric depth, x_0 and z_0 indicate the contrail's central position, and IWC_p stands for the maximum ice water content (IWC) in the center of the contrail. Equation (1) results in a continuous decrease of the IWC for larger radii starting from the maximum IWC_p in the contrail center. The contrail was, according to GH, 400 m thick and located between a height of 9.8 and 10.2 km. Likewise, the contrail was defined with a width of 800 m (i.e., an aspect ratio of 2:1). For the simulations the contrail IWC distribution was defined with a resolution of 8×8 pixels in the x and z directions. Apart from the contrail, the domain was cloud-free. As in GH, a mean contrail optical depth of 0.2 at a wavelength of 550 nm was chosen for this study.

d. Realistic contrails

The sensitivity study for the realistic contrails uses the standard midlatitude summer atmosphere (Anderson et al. 1986). This is combined with meteorological (temperature, density of air, water vapor mixing ratio) and microphysical (IWC, effective ice particle radius) output data from a 2D LES model used for simulation of

persistent contrails (Unterstrasser and Gierens 2010a). The ambient conditions of the contrail simulations are a temperature of 222 K (at formation height) and a relative humidity of 130% (with respect to ice). In Fig. 2 the cross section of the IWC distribution is shown for the (left) sheared and (right) nonsheared contrails for different time steps. The vertical wind shear was either 0 or 0.006 s^{-1}. The contrails were also set up in a 2D domain, now measuring 120 km in the vertical and with periodic boundary conditions in the lateral direction. The bottom of the LES domain is placed in the upper troposphere–lower stratosphere (UTLS) region between 10.5 and 12 km, such that the temperature at the bottom of the LES domain and of the background profile match. Continuity in all vertical profiles is achieved by using linear approximation regions above and below the LES domain. In particular, the water vapor levels in the LES domain (supersaturated in the cloud-free area and around saturation inside the contrail) are higher than the climatological values of the background profile and thus rise (drop) below (above) the contrail layer. More details on how the LES data is incorporated in the background profile can be found in Unterstrasser and Gierens (2010b), where the impact of radiation on the contrail evolution was investigated with an ICA method.

The original LES data have a spatial resolution dx and $dz \approx 10$ m and are averaged onto a coarser grid. The vertical resolution in the contrail layer is 100 m and reduces to 1 km above and below the contrail. For the nonsheared contrail the horizontal resolution is 240 m, whereas in the sheared case it increases from 240 to 1440 m for older contrails in order to reduce computation time (cf. Fig. 2). The domain width used for the radiative transfer calculations depends on the actual width of the contrail, which itself depends on the age (20 min up to 6 h) and the shear conditions. It was chosen to be at least 5 times larger than the contrail width in order to study isolated contrails and prevent interaction of photons between neighboring contrails through the periodic boundaries. The contrail properties are summarized in Table 1. The upper part of the table shows the geometric dimensions and the mean optical depth (OD) of the nonsheared contrail for various time steps, and the lower part contains the same information for the sheared contrail.

In Fig. 3 the time evolution of the contrail mean optical depth is shown for the sheared and the nonsheared contrails as well as the product of the mean optical depth and the contrail width. This quantity is strongly increasing with time for the sheared contrail, whereas it is less pronounced for the nonsheared contrail, for which the product decreases again for later time steps. Generally, the latter quantity is used to measure/compare the radiative impact of contrails evolving in different ambient conditions (relative humidity, temperature, vertical wind shear, stratification, etc.). In Unterstrasser and Gierens (2010b) this quantity is referred to as ''total extinction'' [see their Eq. (12) for a proper definition].

The 2D LES model is based on the nonhydrostatic anelastic Eulerian/semi-Lagrangian fluid solver (EULAG) model (Smolarkiewicz and Margolin 1997; Prusa et al. 2008) coupled with a recent two-moment bulk microphysics scheme (Spichtinger and Gierens 2009), including processes like deposition growth, sublimation, sedimentation, and nucleation. In Unterstrasser and Gierens (2010a) the evolution of contrails and their transition into a contrail cirrus was studied for a large range of atmospheric parameters, also accounting for effects of the early wake–vortex contrail interaction (Unterstrasser et al. 2008).

For the present study we selected two contrail simulations with the highest temperature and relative humidity under investigation. The simulation with no vertical wind shear gives a rather narrow contrail with a strong fall streak. The optical depth drops from initially 0.25 to 0.08 after about 6 h (see Fig. 3, solid line, circles). We want to note that the mean optical depth when evaluated in the LES model can have values twice as large (0.5 for 1000 s, not shown). The reason is that the LES model uses a much finer spatial resolution than the radiative transfer simulation. To obtain the coarse resolution the IWC is averaged over the finer LES grid. For the second simulation, a large shear value of 0.006 s^{-1} was chosen. Therefore, the extension of the contrail is much larger in the horizontal than in the vertical and resembles a thin slightly sheared cloud sheet that is partly subvisual (i.e., $\tau \approx 0.02$). Also for this contrail the mean optical depth steadily decreases with time from 0.16 to 0.06 (see Fig. 3, solid line, diamonds).

3. Simulations and results

Like in the study of GH, the RF in this study was calculated from the difference between the horizontal mean irradiances at top of the atmosphere (at 50- or 120-km altitude, respectively) of clear-sky simulations and simulations with contrail. Thus, a negative RF indicates a cooling and a positive RF a warming of the atmosphere–surface system.

For the approximated 1D calculations with the ICA method the domain was divided up into discrete columns, which are treated as separate, horizontal homogeneous domains of different width; radiative transfer between different columns is not allowed. For completeness, it should be mentioned that this approach is still far more complex than the parameterization of

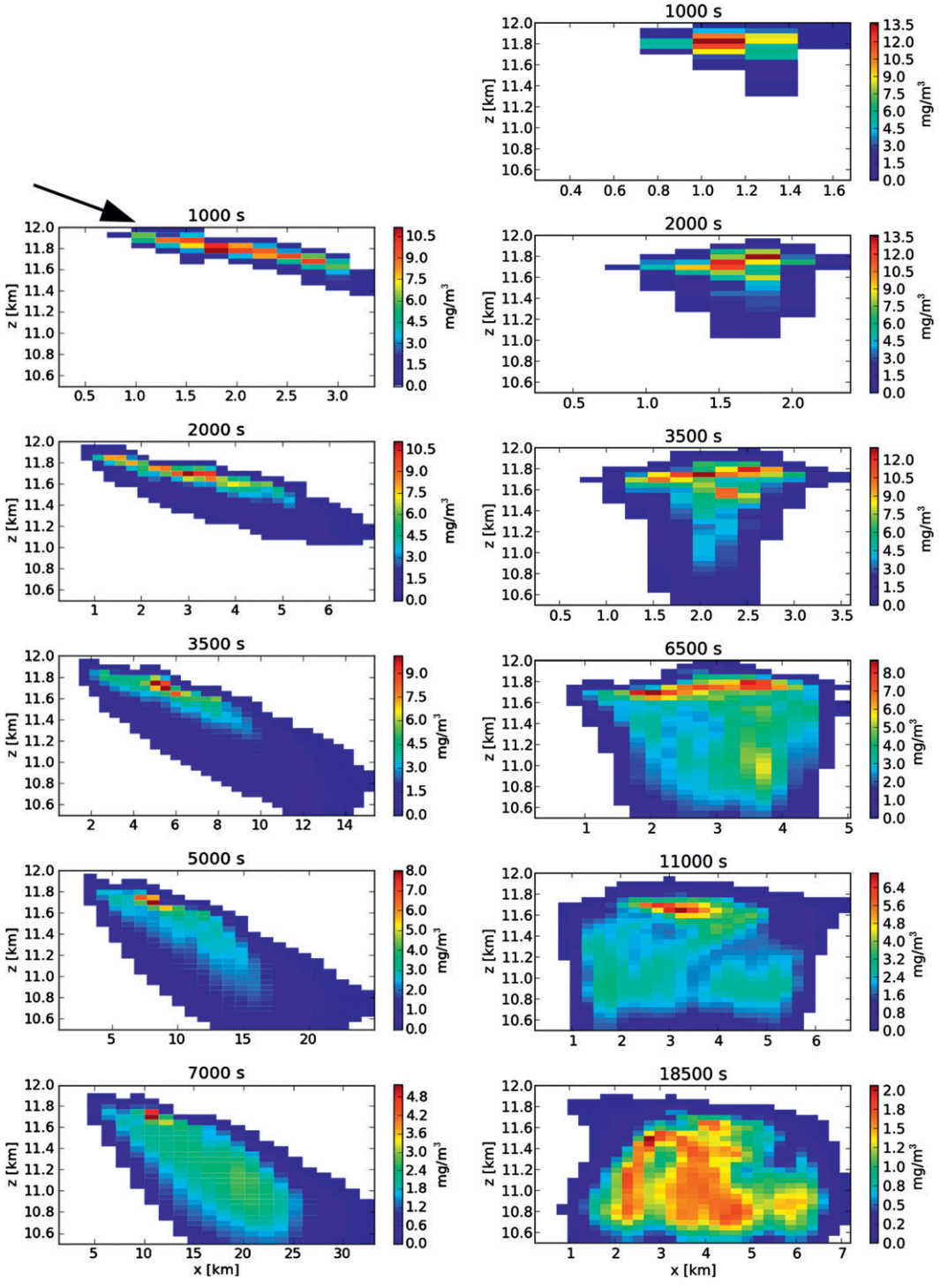

FIG. 2. Cross section of the realistic (left) sheared and (right) nonsheared contrail for all simulation time steps showing the IWC distribution in the x–z plane. For the calculations, the contrail is assumed to be infinitely extended along the y axis. The arrow in the plot of the 1000-s-old sheared contrail marks the incident solar radiation perpendicular to the contrail (i.e., $\phi = 90°$) for an SZA close to the shear angle of the contrail. Note the different spacing of the x and z axes.

TABLE 1. Properties of the nonsheared and sheared realistic contrail for the respective contrail ages.

	Time (s)	Width (km)	Resolution (m)	Contrail thickness (km)	Mean OD
Nonsheared	1000	0.96	240	0.65	0.26
	2000	1.68	240	0.90	0.24
	3500	2.88	240	1.50	0.25
	6500	4.32	240	1.50	0.24
	11 000	6.00	240	1.50	0.17
	18 500	6.48	240	1.45	0.08
Sheared 0.006 s^{-1}	1000	2.64	240	0.60	0.16
	2000	6.24	240	0.90	0.11
	3500	13.92	480	1.50	0.08
	5000	22.08	960	1.50	0.07
	7000	30.24	1440	1.50	0.06

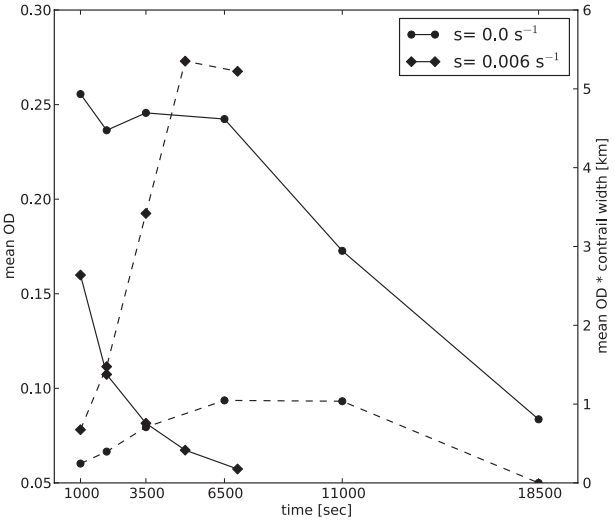

FIG. 3. Realistic contrails: Time evolution of the mean optical depth (solid) and the product of contrail width and mean optical depth (dashed) [for definition, see Eq. (12) of Unterstrasser and Gierens (2010a)], for realistic sheared (diamonds) and nonsheared (circles) contrails.

a GCM, which uses only an average optical depth. This implies that a GCM parameterization is also subject to the plane-parallel bias, which, however, is small for the typical optical depths of contrails.

a. Sensitivity studies with idealized contrail

Figure 4 shows the spatial variation of the (left) shortwave downward and (right) longwave upward irradiances in the 2D domain influenced by the idealized contrail with a mean optical depth of 0.4 for a solar zenith angle of $\theta = 50°$ and a solar azimuth angle of $\phi = 90°$ (i.e., the sun shines perpendicular to the contrail; for a definition, see Fig. 1). To compare the results with GH, we chose the same domain size. The effect of the periodic boundary conditions in MYSTIC is illustrated by the contrail shadow in Fig. 4 (left). Furthermore, the figure shows the decrease of the shortwave radiation toward the ground due to extinction. The decrease of the upward longwave irradiance toward the top of the atmosphere (TOA), especially due to absorption and the additional reduction of the longwave radiation above the cold contrail, is depicted in Fig. 4 (right). Compared to the results of GH (Fig. 2), in the results calculated with MYSTIC no artificial patterns, which arose from the angular discretization in the SHDOM model, are visible.

For ease of comparison with other studies, the results of the simulations in GH were scaled to a contrail cover of 100%. Since the results of GH should be compared with the results of this study, the scaling of the RF values was such that the aligned elliptical contrails would cover the whole domain.

The control experiment, corresponding to GH, was performed for the idealized control contrail described in section 2c (mean optical depth = 0.2), which examines the sensitivity of the contrail RF to a change in the solar zenith angle (SZA). The results are shown in Fig. 5 for the longwave, the shortwave, and the net RF. The longwave 3D effect amounts to 10.4% ± 5.8%. GH state a 3D effect of about 7.5%, which lies within the margin of uncertainty. The 3D longwave RF is, like in GH, larger than the ICA RF. The reason for the increased 3D longwave RF is, as described in GH, that the additional horizontal photon transport enables the contrail to absorb upwelling radiation from lower in the atmosphere at its sides and to emit radiation with a lower intensity (according to the temperature of the contrail) more efficiently than in the 1D case, causing a stronger warming effect in the longwave spectral region.

The shortwave RF shows, in agreement with GH, a strong sensitivity to the SZA. For SZA $< 40°$, the 3D effect in the shortwave range is negligible within the margin of uncertainty in contrast to the results of GH, who state a decrease in the absolute value for the 3D calculations in comparison to the ICA calculations of about 5% respectively, even for small SZAs.

For large SZAs, however, strong effects are visible in Fig. 5, similar to the results of GH. For a laterally illuminated contrail (i.e., $\phi = 90°$), the value of the 3D RF becomes substantially more negative than the ICA RF because the shadow cast by the contrail enlarges and thus results in an enhanced cooling effect in the shortwave. When solar beam and contrail length axis are located in the same plane (i.e., $\phi = 0°$), the additional horizontal photon transport reduces the cooling effect in the shortwave spectral region (i.e., the amount of the shortwave RF, compared to the ICA approximation).

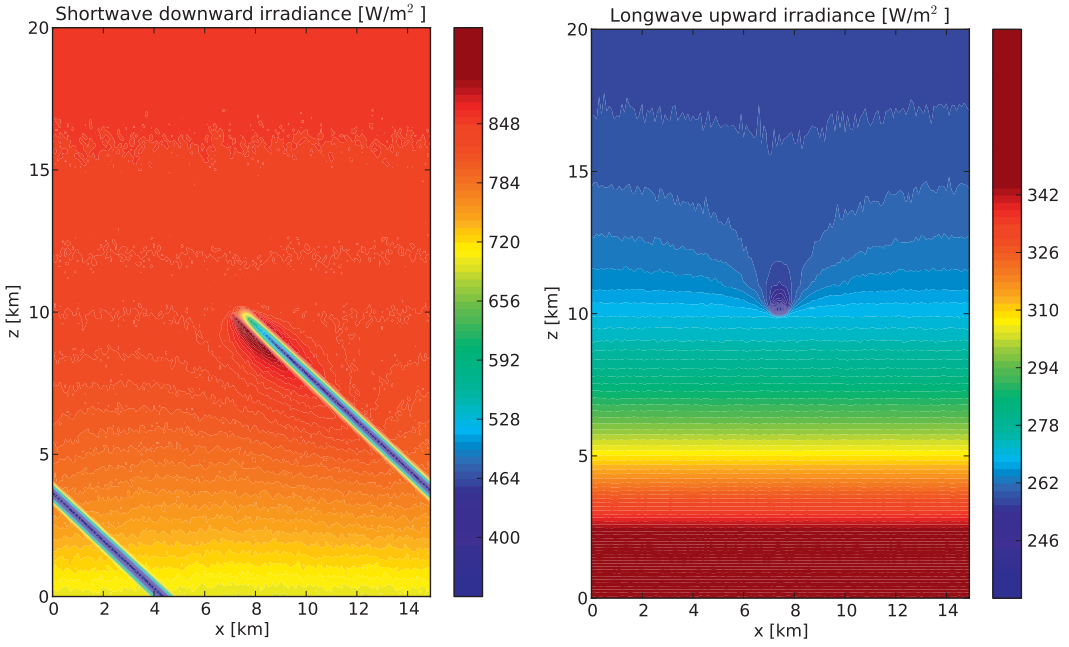

FIG. 4. Spatial variation of the (left) shortwave downward and (right) longwave upward irradiances influenced by the idealized contrail, calculated with MYSTIC. The contrail with dimensions of 400 m in the vertical and 800 m in the horizontal has a mean optical depth of 0.4 at 550 nm and consists of solid hexagonal ice columns. The solar zenith and azimuth angle are set to $\theta = 50°$ and $\phi = 90°$, respectively.

In the case of 3D radiative transfer, the photons, which enter the contrail from above, also have the possibility to exit the contrail through its sides, decreasing the amount of photons reaching TOA, and therefore the absolute value of the RF reduces.

The other three sensitivity studies (doubling of optical depth, variation of aspect ratio, and effective radius) in GH could also be reproduced qualitatively with MYSTIC. However, the increase of the 3D effects in the aspect-ratio experiment was not as distinct as in GH.

Overall, the results of our simulations with the idealized elliptical contrail are very similar to those of GH and the 3D effects are consistent with the findings of GH. Deviations in the absolute values of the RF, however, may arise mainly from the different parameterizations of the ice particles' optical properties (see section 2b): according to Markowicz and Witek (2011), spherical ice crystals (used in GH) cause a stronger RF than hexagonal columns. In the longwave spectrum differences in the absolute RF may also arise from the different mixing ratios of some greenhouse gases (see section 2c). Clearly, also the use of different radiative transfer models for the calculation of the 3D effects can be responsible for the differing absolute RF. Since two completely different approaches to the solution of radiative transfer have been applied in the two studies, the results can be considered reliable.

b. *Sensitivity studies with realistic contrails*

For the two time series of both the sheared and the nonsheared realistic contrail, calculations were made for several SZAs and two azimuth angles ($\phi = 0°$ and $\phi = 90°$) each. For ease of comparison, the results of the following experiments were scaled to a contrail cover of 100% as well.

1) NONSHEARED CONTRAIL

Figure 6 shows the sensitivity of the longwave, shortwave, and net RF at TOA to the SZA of the nonsheared contrail at 1000 s. In comparison to the idealized contrail (see Fig. 5), the main characteristics of the curves and the basic dependence on SZA are very similar, although the absolute values of the forcings are larger for the present case. The longwave RF is 29.7 ± 0.2 W m^{-2} for the ICA calculation, and thus larger than for the idealized contrail with 18.2 ± 0.7 W m^{-2} (ICA). This occurs mainly because the realistic contrail is located more than 1 km higher in the atmosphere at colder temperatures and therefore the outgoing longwave radiation is reduced. Another reason is the different temperature and water vapor mixing ratio profiles (see section 2d), which contribute to an enhanced longwave RF. The additional horizontal photon transport causes a longwave 3D effect of 7.6% ± 0.7%. This value is

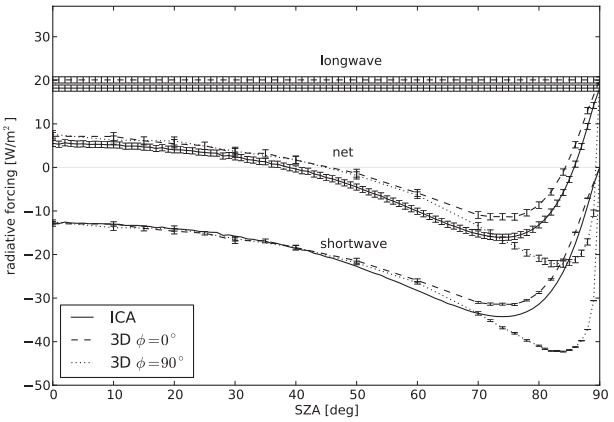

FIG. 5. Sensitivity of RF of control (idealized) contrail ($\tau = 0.2$; $r_{\text{eff}} = 10$ μm; 800 m $\times$ 400 m; solid columns) to SZA at TOA calculated with MYSTIC. The upper two lines show the longwave RF, the lowermost lines the shortwave, and the lines in the middle represent the net RF. The solid lines depict the results from the ICA calculations; dotted and dashed lines show the values for the 3D calculations with $\phi = 0°$ and $\phi = 90°$, respectively. For the meaning of ϕ, see Fig. 1. For the longwave component, only the dashed line is plotted since it is identical to the dotted line.

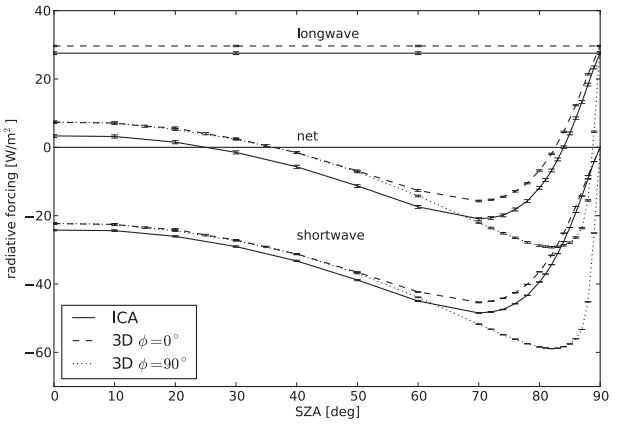

FIG. 6. As in Fig. 5, but for realistic nonsheared contrail.

slightly smaller than for the idealized contrail with 10.4% ± 5.8%, which can be attributed to the smaller aspect ratio of the realistic contrail (about 3:2) compared to the idealized contrail (2:1). Also in the shortwave spectrum the negative RF of -24.2 ± 0.2 W m^{-2} (ICA at SZA = 0°) is larger than for the simulation with the idealized contrail with -12.7 W m^{-2}. This is caused by various effects. First, the slightly larger mean optical depth of the realistic contrail with 0.26 compared to 0.2 for the idealized contrail. Second, the realistic contrail is about 160 m wider than the idealized contrail and hence reduces the incident shortwave radiation to a larger extent. Third, the effective radii of the ice particles in the realistic contrail are on average larger (about 18 μm for 1000 s) than for the idealized contrail (10 μm). As a result, the average asymmetry parameter of the ice particles increases and enhances forward scattering, which reduces the amount of the shortwave upward flux. The shortwave 3D effect, which was negligible in the case of the idealized contrail, is significant for the realistic contrail. In the latter case, the additional horizontal photon transport decreases the absolute value of the shortwave RF about 8.1% ± 0.7%. The two contributions of the 3D effect in the shortwave and the longwave spectral range add up to a net 3D effect of 4.1 ± 0.5 W m^{-2} or about 122.0% ± 10.1% for a SZA of 0° and an azimuth angle of 90°, which is also larger than for the idealized contrail (about 37.1% ± 23.5%). It should be noted that the relative 3D effect for this SZA is very large because the shortwave and longwave RF nearly cancel.

Figure 7 depicts the time evolution of the longwave, shortwave, and net RF at TOA for three different solar zenith angles. The longwave RF is, of course, identical for the three SZAs. Basically, the absolute values of the longwave and the shortwave RF decrease with contrail age in all cases, since the contrail mean optical depth diminishes with age (see Fig. 3) because of horizontal stretching and sedimentation. For SZA = 0° the net 3D effect, starting with ΔRF = 120% of the ICA RF for the first time step (1000 s), decreases with contrail age since horizontal photon transport is less likely in an optically thinner contrail. The 3D effect is similar for SZA = 40° and the net RF is larger using the 3D model. However, more interesting is the fact that the net forcing changes its sign over the contrail's life cycle. The once-cooling contrail has a warming effect at later stages. For a large zenith angle of 80° the 3D effect is more diverse and depends also strongly on the azimuth angle. Contrary to SZA = 0° and SZA = 40°, the net RF calculated with the 3D model can be smaller than that of the ICA model.

2) SHEARED CONTRAIL

Figure 8 illustrates the sensitivity of the RF to the solar zenith angle at TOA of the sheared contrail. In contrast to the corresponding Figs. 5 and 6, no 3D effect is apparent for smaller SZAs. Two effects account for this. On the one hand, the strong wind shear quickly stretches the contrail in horizontal direction, reducing its optical depth. On the other hand, the spreading enlarges the aspect ratio (i.e., the ratio between the top or bottom areas and the contrail sides relative to the vertical axis). Apart from that, it can be seen in Fig. 8 that the amount of the longwave RF (17.7 ± 0.5 W m^{-2}, ICA) as well as the absolute value of the shortwave RF (-11.9 ± 0.3 W m^{-2}, ICA) are smaller compared to the nonsheared contrail in Fig. 6. Since both are located at

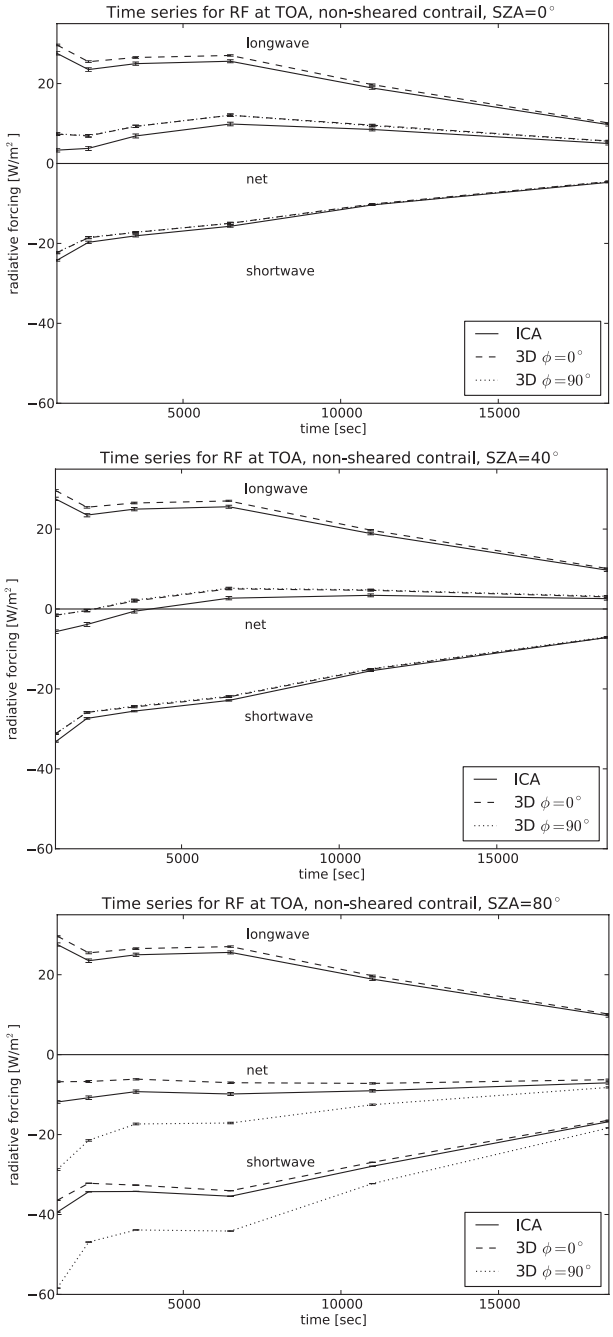

FIG. 7. As in Fig. 6, but for the time evolution of the realistic nonsheared contrail's RF for solar zenith angles of $\theta = 0°, 40°$, and 80°.

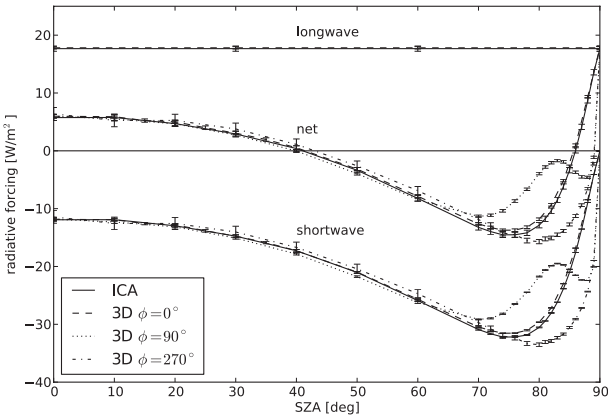

FIG. 8. As in Fig. 5, but for realistic sheared contrail. Dotted, dashed, and dash-dotted lines show the values for the 3D calculations with $\phi = 0°$, $\phi = 90°$, and $\phi = 270°$, respectively. For the longwave component, only the dashed line is plotted since the other two lines are identical.

the same height (see Table 1), the smaller longwave RF of the sheared contrail can mainly be attributed to the substantially lower optical depth of 0.16 compared to 0.26 for the nonsheared contrail. The differing optical depth is primarily caused by a lower IWC since the mean effective ice particle radius for both contrails is approximately the same (18.2 μm nonsheared vs 19.5 μm sheared contrail). Therefore, the smaller absolute value of the shortwave RF for the sheared contrail is also mainly due to the lower optical depth.

For large SZAs a local maximum in the shortwave RF can be found, which is caused by the sheared geometry of the contrail. For illustration see the 1000-s contrail in Fig. 2 (left), where an arrow marks the direction of the incident sunlight. The peak in the shortwave RF can be explained with the time evolution of the shadow cast by the contrail, which is minimal for a SZA close to the shear angle of the contrail. Thus also the absolute value of the shortwave RF exhibits a minimum for these SZAs, which range for the contrails in this study from about 77° for 1000 s up to about 87° for the last time step at 7000 s, and occurs only for the simulations where the sun is perpendicular to the contrail but not in the parallel case. Generally the shear of the contrails depends on the magnitude of the vertical wind shear and on their age. Therefore, this local maximum occurs at even larger SZAs for older contrails as their shear increases. From numerical simulations and lidar observations, it is known that contrails usually grow faster in the horizontal than in the vertical direction and have a large aspect ratio. The linear shape that is characteristic of evolving contrails might be a prominent feature compared to naturally formed cirrus and can also be discovered in other numerical simulations (see plates 3 and 4 of Jensen et al. 1998) and lidar observations (see Fig. 2 of Freudenthaler et al. 1995).

For (nearly) symmetric contrails, like the idealized and the nonsheared contrail, it is sufficient to vary the SZA from 0° to 90° in order to examine all possible positions of the sun. The sheared contrail, however, has a strongly nonsymmetric shape across the vertical axis.

Thus, the sensitivity to the solar zenith angle should actually be studied for the total half-space. As an example, the sensitivity of the contrail RF to the SZA was examined at a solar azimuth angle of $\phi = 270°$ for a contrail age of 1000 s (see dash-dotted line in Fig. 8). For this mirrored setup, the peak in the shortwave RF did not appear for large SZAs and the position of the sun perpendicular to the contrail plane, since the contrail was illuminated from the opposite side.

Figure 9 depicts the RF of the sheared contrail as a function of time again for three SZAs. Clearly, for $\theta = 0°$ the 3D effect, which can be neglected already for the first time step at 1000 s, remains negligible also for older contrails. Similar to the behavior of the RF for the nonsheared contrail in Fig. 7, the amount of the longwave RF as well as the absolute value of the shortwave RF is decreasing for older contrails for reasons of a reducing contrail optical depth. For $\theta = 0°$, similarly, the net forcing is positive and no 3D effect is apparent. Like for the nonsheared contrail, the net forcing of the sheared is negative for a large zenith angle of 80°. Only for a laterally illuminated contrail ($\phi = 90°$) a substantial 3D effect can be expected. Interestingly, the 3D model yields a less negative net forcing, since the SZA, for which the results are shown here, lies in the range where the local maximum of the 3D shortwave RF occurs.

In a further test we checked whether the reduced 3D effect in the sheared case could partly be attributed to the coarser horizontal resolution, used for the later time steps. We picked two configurations with a sheared contrail where the 3D effect was apparent for the default horizontal resolution. Thus, the sheared contrails at the two contrail ages 3500 s (resolution = 480 m) and 5000 s (resolution = 960 m) were both calculated at a resolution of 240 m for a SZA of $\theta = 80°$. The deviations in the RF were negligible: For the contrail at 3500 s the deviation between the shortwave 3D effects for resolutions of 480 and 240 m amounts to 0.0001 ± 0.0285 W m^{-2} for $\phi = 90°$ and 0.0033 ± 0.0279 W m^{-2} for $\phi = 0°$, which can be neglected within the margin of uncertainty. For the contrail at 5000 s the deviations between the shortwave 3D effects at resolutions of 240 and 960 m, respectively, were also negligible with about 0.0014 ± 0.0257 W m^{-2} for $\phi = 90°$ and 0.0040 ± 0.0252 W m^{-2} for $\phi = 0°$. Therefore, it can be assumed that the 3D effect remains unaffected by our choice of the resolution. Also the results of the shortwave RFs for the respective resolutions remain the same within the margin of uncertainty for both contrail ages.

Considering the two realistic contrail evolutions, the absolute values of the longwave and shortwave forcing of the sheared are generally smaller than those of the nonsheared contrail, simply because of the smaller optical depth. So far the RFs of the contrails have all been scaled to a contrail cover of 100% for ease of comparison with other studies. To conclusively compare the radiative effects of individual contrails (per flight meter), the RFs have to be integrated along the transverse direction (i.e., the x axis in Fig. 1) over the total width of the domain. Then, for identical background conditions the sheared contrail generally exerts

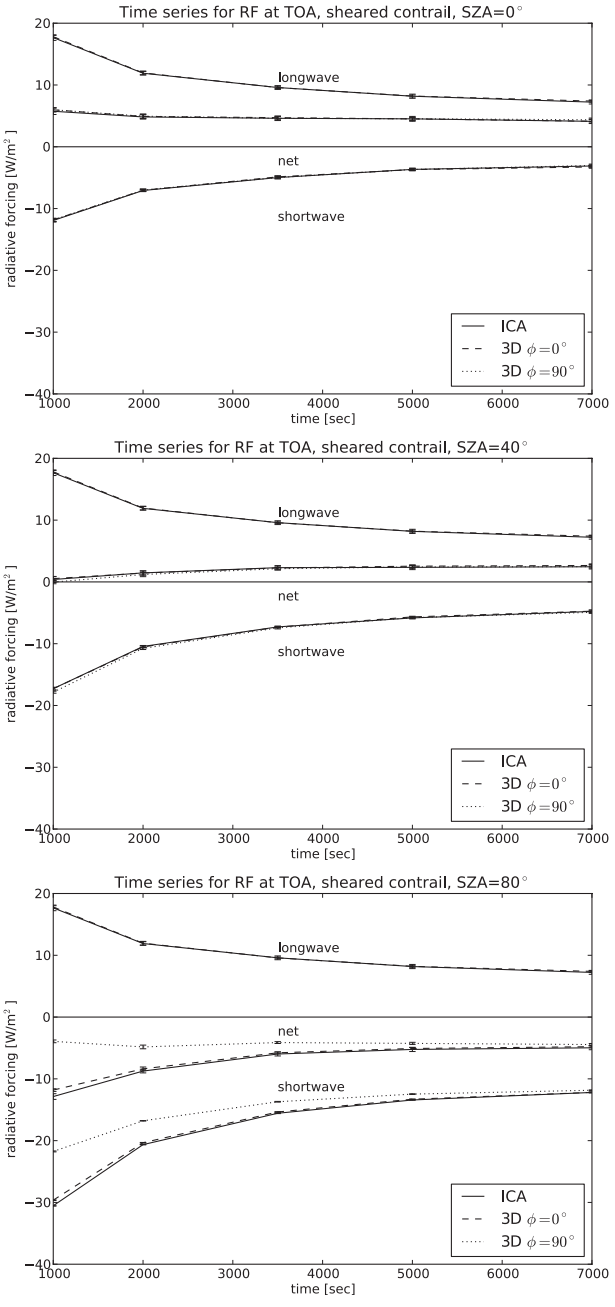

FIG. 9. As in Fig. 8, but for the time evolution of the realistic sheared contrail's RF for solar zenith angles of $\theta = 0, 40°$, and 80°.

a stronger RF per flight meter, similarly to the product of contrail width and mean optical depth as shown in Fig. 3.

3) REGULARLY ARRANGED CONTRAIL CLUSTER

In all preceding simulations the overall domain width was chosen to be at least 5 times larger than the contrail width in order to assure negligible radiative interactions between neighboring contrails via the periodic boundary. In reality, however, contrails also appear in clusters and radiative interactions between contrails may occur. Thus, in the following experiments small domain widths are prescribed and the contrails lie closer together. This mimics a very simple cluster with all contrails having the same orientation, separation distance, and age.

At 11 000 s the nonsheared contrail has a width of 6 km. We reduced the original width of the domain from 30 to 9 km. Identically, the 14-km-wide sheared contrail at 3500 s was examined in a 14-km-wide domain instead of 70 km. For the latest case no rescaling of the RF was necessary to obtain a contrail cover of 100% since the contrail already covered the whole domain. The simulations with the 3D model show that for smaller SZAs the RFs as well as the 3D effects are almost unaffected by the choice of the domain width within the margin of uncertainty (see Fig. 10). Considering the incoming solar radiation perpendicular to the contrail plane ($\phi = 90°$), the absolute value of the 3D solar RF is slightly larger for the contrail cluster than for the single contrail for larger SZAs. For $\theta = 80°$ the absolute value of the 3D solar RF for the sheared contrail cluster is about 0.088 ± 0.055 W m^{-2} larger than the individual contrail. For the nonsheared contrail cluster the absolute value of the 3D solar RF is about 0.336 ± 0.047 W m^{-2} larger than for the single contrail for the same SZA. This is because of the multiple interactions of the solar photons with the contrail (i.e., the contrail cluster) for larger zenith angles. Because of multiple scattering the probability of a photon of being scattered into the upper half space increases and thus the shortwave RF rises as well. For very low positions of the sun (i.e., large SZAs), however, a slight reduction of the absolute 3D solar RF for $\phi = 90°$ results in both sheared and the nonsheared contrail clustering in comparison to the single contrails. This test represents another step toward more realism. In reality, the photon paths may be even more intricate since the contrails' orientations and cross-sectional areas are more variable. Furthermore, the characteristic peak in the shortwave RF found for the isolated sheared contrail smears out for the contrail cluster (see Fig. 11). This effect is expected to be even more pronounced for a heterogeneous contrail cluster since the individual contrail sheets are likely to have differing shear angles.

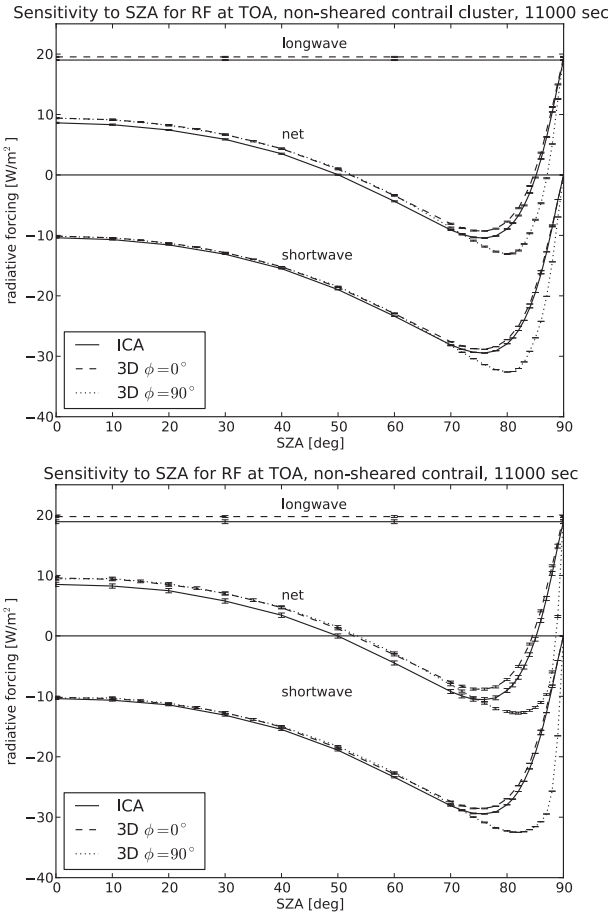

FIG. 10. As in Fig. 8, but for the RF of the nonsheared contrail cluster and single contrail.

4. Summary and conclusions

So far Schulz (1998) and Gounou and Hogan (2007, herein GH) have examined the 3D effects of idealized contrails. To our knowledge, no other publications have accounted for horizontal photon transport since they applied the plane-parallel approximation. Using a setup as close as possible to this of GH we obtained comparable results for the 3D effects of the idealized contrail of about 10% for the longwave and shortwave RFs, respectively. Further sensitivity studies showed that the results of GH could be reproduced qualitatively with the MYSTIC model and that the 3D effects of both studies are comparable.

In the main part of our study the sensitivity of the RF to the SZA was examined for different time steps in the life cycle of a sheared and a nonsheared realistic contrail. In the case of the nonsheared contrail, significant

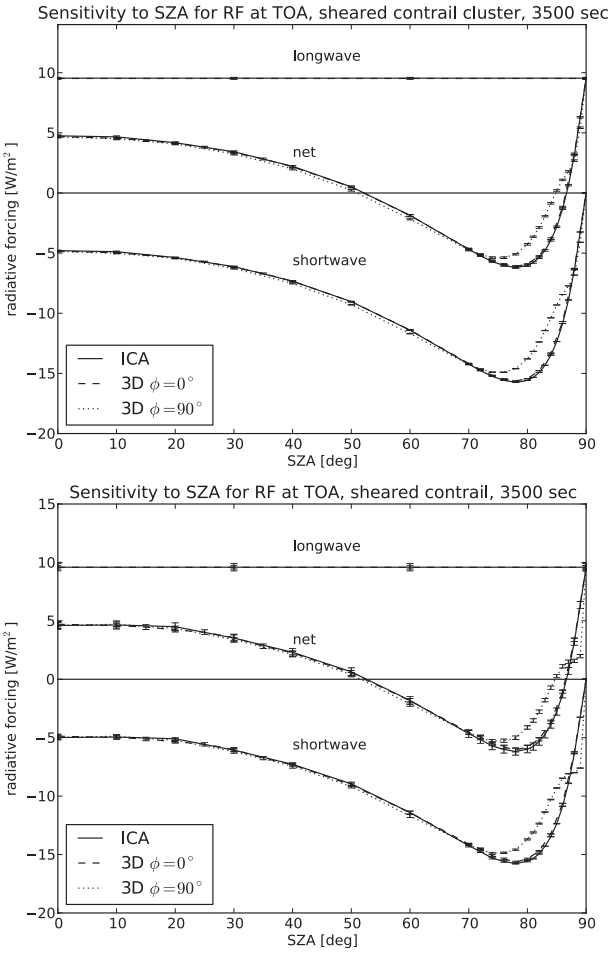

FIG. 11. As in Fig. 8, but for the RF of sheared contrail cluster and single sheared contrail.

3D effects occur for the shortwave RF (about 8.1% for $\phi = 90°$ and $\theta = 0°$) as well as for the longwave RF (about 7.6%) for a contrail age of about 20 min. Both effects add up to a pronounced net 3D effect of about 122% for $\phi = 90°$ and $\theta = 0°$. The large relative 3D effect occurs because the longwave and the shortwave RF nearly cancel and the net RF is small compared to both contributions. For older contrails, the 3D effect remains significant, yet decreases continuously as the mean optical depth of the spreading contrail diminishes. Interestingly, the net RF changes sign over the contrail's life cycle for selected SZAs. For the sheared as for the nonsheared contrail a decrease in the longwave RF and the absolute value of the shortwave RF can be observed over time. However, the 3D effect for the sheared contrail is negligible within the margin of uncertainty. As a further step toward more realism, we examined the behavior of the RF for regularly arranged contrail clusters for the sheared and nonsheared contrails. We found small deviations in the 3D shortwave RF, which was slightly larger for the contrail cluster compared with the single contrail for larger SZAs.

All simulations demonstrate that the 3D effects of contrails are very sensitive to changes in the optical depth, the aspect ratio and the effective radius of the ice crystals. Despite the fact that the 3D effects in the shortwave and the longwave spectrum are small, they add up in the net RF and it revealed that the effect of horizontal photon transport in contrails, especially for larger SZAs, is not negligible. Thus, contrail radiation studies focusing on the polar region or accounting for the diurnal cycle may include 3D effects since they are largest for low elevations of the sun. Since realistic contrails can show diverse distributions of IWC, ice particle sizes, and shapes together with different aspect ratios, they cause a more or less pronounced 3D effect. As the simulations have shown in this study, the 3D effects change not only from one contrail to the other but also along its temporal evolution.

GH suggest a parameterization of the 3D effects for contrails. The simulations of realistic contrails performed in this study reveal that a parameterization of the 3D effects should include both the geometry and the microphysics of the contrail since they determine the radiative 3D effects of the contrail and influence each other. Wind shear acting on a contrail affects its shape and orientation but also its optical depth and the particle size. Marshall (1953) and Hogan and Kew (2005) showed that the shape of cirrus uncinus fall streaks can be predicted by knowing the shear and fall speed of the ice particles. This is essentially the same as predicting the orientation of a sheared contrail.

Even though both studies show that the 3D effects are not negligible, further uncertainties occur with RF calculations in contrails, such as the parameterization of the optical depth, the ice particles, or the IWC of the contrail. These are at least of the same magnitude as the differences between the ICA and 3D calculations and the 3D effects should be considered along with the improvements of the other mentioned uncertainties.

Acknowledgments. We thank Ulrich Schumann for initiating this study and for helpful discussions. Special thanks also to Michael Ponater for proofreading this paper and for his useful comments. Robert Buras and Tobias Zinner also supported this work with valuable comments and ideas.

REFERENCES

Anderson, G., S. Clough, F. Kneizys, J. Chetwynd, and E. Shettle, 1986: AFGL atmospheric constituent profiles (0–120 km). Air Force Geophysics Laboratory Tech. Rep. AFGL-TR-86-0110, 43 pp.

Burkhardt, U., and B. Kärcher, 2009: Process-based simulation of contrail cirrus in a global climate model. *J. Geophys. Res.,* **114,** D16201, doi:10.1029/2008JD011491.

——, and ——, 2011: Global radiative forcing from contrail cirrus. *Nature Climate Change,* **1,** 54–58, doi:10.1038/nclimate1068.

Emde, C., and B. Mayer, 2007: Simulation of solar radiation during a total eclipse: A challenge for radiative transfer. *Atmos. Chem. Phys.,* **7,** 2259–2270.

Evans, K., 1998: The spherical harmonics discrete ordinate method for three-dimensional atmospheric radiative transfer. *J. Atmos. Sci.,* **55,** 429–446.

Freudenthaler, V., F. Homburg, and H. Jäger, 1995: Contrail observations by ground-based scanning lidar: Cross-sectional growth. *Geophys. Res. Lett.,* **22,** 3501–3504.

Frömming, C., M. Ponater, U. Burkhardt, A. Stenke, S. Pechtl, and R. Sausen, 2011: Sensitivity of contrail coverage and contrail radiative forcing to selected key parameters. *Atmos. Environ.,* **45,** 1483–1490.

Fu, Q., and K. N. Liou, 1993: Parameterization of the radiative properties of cirrus clouds. *J. Atmos. Sci.,* **50,** 2008–2025.

Gounou, A., and R. J. Hogan, 2007: A sensitivity study of the effect of horizontal photon transport on the radiative forcing of contrails. *J. Atmos. Sci.,* **64,** 1706–1716.

Hogan, R. J., and S. F. Kew, 2005: A 3D stochastic cloud model for investigating the radiative properties of inhomogeneous cirrus clouds. *Quart. J. Roy. Meteor. Soc.,* **131,** 2585–2608.

Jensen, E., A. Ackerman, D. Stevens, O. Toon, and P. Minnis, 1998: Spreading and growth of contrails in a sheared environment. *J. Geophys. Res.,* **103** (D24), 31 557–31 568.

Kärcher, B., U. Burkhardt, S. Unterstrasser, and P. Minnis, 2009: Factors controlling contrail cirrus optical depth. *Atmos. Chem. Phys.,* **9,** 6229–6254.

Kato, S., T. P. Ackerman, J. H. Mather, and E. Clothiaux, 1999: The *k* distribution method and correlated-*k* approximation for a shortwave radiative transfer model. *J. Quant. Spectrosc. Radiat. Transfer,* **62,** 109–121.

Key, J. R., P. Yang, B. A. Baum, and S. L. Nasiri, 2002: Parameterization of shortwave ice cloud optical properties for various particle habits. *J. Geophys. Res.,* **107,** 4181, doi:10.1029/2001JD000742.

Markowicz, K. M., and M. L. Witek, 2011: Simulations of contrail optical properties and radiative forcing for various crystal shapes. *J. Appl. Meteor. Climatol.,* **50,** 1740–1755.

Marshall, J. S., 1953: Precipitation trajectories and patterns. *J. Meteor.,* **10,** 25–29.

Mayer, B., 2009: Radiative transfer in the cloudy atmosphere. *Eur. Phys. J. Conf.,* **1,** 75–99, doi:10.1140/epjconf/e2009-00912-1.

——, and A. Kylling, 2005: Technical Note: The libRadtran software package for radiative transfer calculations—Description and examples of use. *Atmos. Chem. Phys.,* **5,** 1855–1877.

McClatchey, R. A., R. A. Fenn, J. E. A. Selby, P. E. Voltz, and J. S. Garing, 1972: Optical properties of the atmosphere. Air Force Cambridge Research Laboratories Environmental Research Paper 411, 113 pp.

Myhre, G., and Coauthors, 2009: Intercomparison of radiative forcing calculations of stratospheric water vapour and contrails. *Meteor. Z.,* **18,** 585–596.

Ponater, M., S. Marquart, and R. Sausen, 2002: Contrails in a comprehensive global climate model: Parameterization and radiative forcing results. *J. Geophys. Res.,* **107,** 4164, doi:10.1029/2001JD000429.

Prusa, J., P. Smolarkiewicz, and A. Wyszogrodzki, 2008: EULAG, a computational model for multiscale flows. *Comput. Fluids,* **37,** 1193–1207.

Rap, A., P. Forster, A. Jones, O. Boucher, J. Haywood, N. Bellouin, and R. De Leon, 2010: Parameterization of contrails in the UK Met Office Climate Model. *J. Geophys. Res.,* **115,** D10205, doi:10.1029/2009JD012443.

Schulz, J., 1998: On the effect of cloud inhomogeneity and area averaged radiative properties of contrails. *Geophys. Res. Lett.,* **25,** 1427–1430.

Smolarkiewicz, P., and L. Margolin, 1997: On forward-in-time differencing for fluids: An Eulerian/semi-Lagrangian nonhydrostatic model for stratified flows. *Numerical Methods in Atmospheric and Oceanic Modelling: The André J. Robert Memorial Volume,* C. Lin, R. Laprise, and H. Ritchie, Eds., Canadian Meteorological and Oceanographical Society, 127–152.

Spichtinger, P., and K. M. Gierens, 2009: Modelling of cirrus clouds. Part 1a: Model description and validation. *Atmos. Chem. Phys.,* **9,** 685–706.

Thomas, G. E., and K. Stamnes, 1999: *Radiative Transfer in the Atmosphere and Ocean.* Vol. 1. Cambridge University Press, 517 pp.

Unterstrasser, S., and K. Gierens, 2010a: Numerical simulations of contrail-to-cirrus transition—Part 1: An extensive parametric study. *Atmos. Chem. Phys.,* **10,** 2017–2036.

——, and ——, 2010b: Numerical simulations of contrail-to-cirrus transition—Part 2: Impact of initial ice crystal number, radiation, stratification, secondary nucleation and layer depth. *Atmos. Chem. Phys.,* **10,** 2037–2051.

——, ——, and P. Spichtinger, 2008: The evolution of contrail microphysics in the vortex phase. *Meteor. Z.,* **17,** 145–156.

Yang, P., K. Liou, K. Wyser, and D. Mitchell, 2000: Parameterization of the scattering and absorption properties of individual ice crystals. *J. Geophys. Res.,* **105** (D4), 4699–4718.

——, H. Wei, H.-L. Huang, B. A. Baum, Y. X. Hu, G. W. Kattawar, M. I. Mishchenko, and Q. Fu, 2005: Scattering and absorption property database for nonspherical ice particles in the near-through far-infrared spectral region. *Appl. Opt.,* **44,** 5512–5523.